Porous copper template from partially spark plasma-sintered Cu–Zn aggregate via dezincification

M MANDAL[1], D SINGH[1], GOUTHAMA[1], B S MURTY[2], S SANGAL[1] and K MONDAL[1,*]

[1]Department of Materials Science and Engineering, Indian Institute of Technology Kanpur,
Kanpur 208 016, India
[2]Department of Metallurgical and Materials Engineering, Indian Institute of Technology Madras,
Chennai 600 036, India

Abstract. Present work deals with the preparation of spark plasma-sintered Cu–Zn aggregate (5, 10 and 20 wt% Zn) with interfacial bonding only starting from elemental powders of Cu and Zn (99·9% purity) and subsequently making of porous template of Cu by dezincification. Sintering is done so as to achieve only interfacial bonding with the aim to maintain maximum potential difference between the Cu and Zn particles during dezincification process in various solutions, viz. 1 N HCl and 3·5 wt% NaCl solutions. X-ray diffraction, optical microscopy and SEM–EDS are carried out to examine microstructural evolution and subsequent changes in hardness with sintering temperatures and different Zn percentages. Dezincification and pore formation are conducted on sintered 0·5 mm thick 12 mm diameter disc samples. The size, distribution and nature of pores in porous templates of Cu are then investigated using optical microscopy and SEM–EDS analysis.

Keywords. Metal; corrosion; porous structure; sintering; powder metallurgy.

1. Introduction

De-alloying of Zn or dezincification in brass is a commonly noticed corrosion phenomenon (Gladen *et al* 1990; Jagodzinski *et al* 2000; Karpagavalli and Balasubramaniam 2007). Several researchers have studied dezincification and suggested different mechanisms based on dissolution of active metal ions (Pickering and Wagner 1967), inter-diffusion (Pickering and Wagner 1967) and percolation theory (Sieradzki and Newman 1986; Newman *et al* 1988). The result of the dezincification is the formation of loosely bound porous highly Cu-enriched layer on the surface of brass (Tuck *et al* 2010). On the other hand, de-alloying process is used effectively to produce nano-porous components useful in applications like catalysis, fuel cells, sensor, actuators, etc (Rintoul *et al* 1996; Bond and Thompson 1999; Joo *et al* 2001; You *et al* 2003). Dezincification has been used to make porous Ag, Pt and Au templates (Huang and Sun 2004; Yeh *et al* 2006; Jia *et al* 2007a, b). It is understood that processing of samples before electrochemical de-alloying (Zhang *et al* 2009) and choice of solution (Zhang *et al* 2012) are important factors for deciding the microstructure and thickness of the de-alloyed layer. Recently, Zhang *et al* (2012) have shown that melt spun Zn–Ag alloy ribbons of

varied composition can form ~ 50 μm thick de-alloyed nano-porous Ag sheet in NaCl and HCl solutions. It is clear from their work as well as from works of other researchers (Huang *et al* 2004; Yeh *et al* 2006; Jia *et al* 2007a, b) that metallurgically prepared samples have the advantage of being made into thicker porous sheet. Moreover, all the previous studies (Huang and Sun 2004; Yeh *et al* 2006; Jia *et al* 2007; Li *et al* 2010; Zhang *et al* 2012) on the making of porous templates are from the precursors consisting of alloys made by either electrochemical deposition or melt spinning. Selective leaching from a binary component undergoing anodic dissolution is most effective, since there exists a large difference in the single-electrode potential of the constituent metals as well as in the case, when the overall electrode potential of the final alloy is significantly lower than that of the more noble component and higher than that of the less noble component (Ahmed and Macdonald 2012). Cu redeposition would further maximize the potential gradient between cathodic and anodic sites in the corrosive solution.

Cast and wrought brasses are most common due to the difficulties in production of PM brasses through conventional PM techniques (pressing and sintering) because of the very fast evaporation of highly volatile Zn during sintering, resulting in high amount of residual porosity and non-uniformity in composition (Radomyselskii *et al* 1984). This heterogeneity problem is, to some extent,
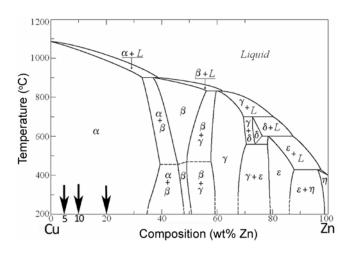
*Author for correspondence (kallol@iitk.ac.in)

overcome by using Cu powders pre-alloyed with Zn. But in that process, extensive Cu–Zn alloying would lead to the formation of several inter-metallic compounds which may affect the mechanical and electrochemical properties of the final product. Efforts have also been made to produce fully-dense brass product by the addition of alloying elements (Shufeng *et al* 2011a, b). Spark plasma sintering (SPS) can be a very novel technique of consolidation of metal powders which completely eliminates the problem of Zn loss due to evaporation using a pulsed d.c. power and uni-axial pressure providing a very high heating rate resulting from plasma and Joule heating and rapid sintering at a relatively low temperature (Hungria *et al* 2009). Recent researches on consolidation of Zn alloys (Gutmanas 1990; Hisashi *et al* 2010; Shufeng *et al* 2011a, b) show the extensive and successful use of SPS technique in eliminating any variation in composition.

In the present work, a novel attempt is made to obtain porous template from partially sintered Cu–Zn aggregate made by spark plasma sintering followed by selective dissolution of Zn in HCl and NaCl solutions. Pure Cu and Zn powders of 99·9% purity are ball milled at low rpm for making homogeneous mixer (no alloying). These mechanically mixed powders are then sintered in such a manner, so that interface bonding takes place only and complete alloying is prevented. The main objective to make such sample is to enhance the potential difference during electrochemical dissolution of Zn from the sintered aggregate and finally, produce porous Cu template.

2. Experimental

Based on binary alloy phase diagram (figure 1) (http://people.virginia.edu/~lz2n/mse305/notes/PD-Binary.pdf), three different compositions of Cu–Zn mixtures were chosen such that the mixtures were within the solid solution range, both at room temperature and at elevated temperatures. Electrolytically prepared Zn powder (99·9% pure, density 7·13 g/cm^3) and Cu powder (99·5% pure, density 8·96 g/cm^3) were then milled in a planetary ball mill at 200 rpm for 45 min to prepare three sets of powders having compositions Cu–5 wt% Zn, Cu–10 wt% Zn and Cu–20 wt% Zn. Milling was carried out using tungsten carbide vials and tungsten carbide balls of 10 mm diameter in a dry atmosphere with a ball to powder ratio of 10 : 1. The powdered samples were finally consolidated to 5 × 12 mm pellets in a graphite die followed by sintering under an uniaxial load of 3·5 kN at three different temperatures of 500, 550 and 600 °C for 5 min, each using a SPS apparatus (Dr Sinter 5000 Series, Model SPS-625, SPS Syntex Inc., Japan). The heating rate was maintained at 100 °C/min to reach sintering temperature and load was applied before the start of the heating and withdrawn after holding the sample at the sintering temperature. The samples were then furnace cooled up to 200 °C followed by air cooling to room temperature. X-ray diffraction using CuKα radiation ($\lambda = 0.15418$ nm) was carried out after ball milling and sintering and the peaks were compared to the standard peaks using PCPDFWIN software. Density of the pellets was measured by Archimedes method. Sinterability of the pellets was calculated using the following equation:

$$\text{Sinterability} = \text{Experimental density of aggregate/theoretical density of aggregate.}$$

Optical microscopy (Zeiss Axio M1m) and scanning electron microscopy (SEM ZEISS EVO 50) were carried out for microstructural characterization of the sintered samples. Metallographic samples were prepared by polishing on 400 to 2000 grit SiC paper followed by cloth polishing using 5 μm alumina and finally, etching in FeCl$_3$ solution for 3–5 s. SEM equipped with energy dispersive X-ray spectrometer (EDS) was used for compositional analysis including the line scan, spot scan and elemental mapping to study the degree of uniformity and distributions of the different constituents. Bulk hardness was measured using the vickers indent by applying a load of 10 g for 15 s and minimum 20 indentations were recorded for each sample at random places in order to have a representative average value of hardness.

For dezincification studies, 0·5 mm thick discs were sliced out from sintered pellets of 12 mm diameter. Direct immersion tests were carried out by suspension of each of the fine polished samples (up to 1600 grit size) in separate conical flasks containing 250 mL of two different types of non-agitated solutions 1 M HCl (pH 0·47) and 3·5 wt% NaCl (pH 7·2) for 45 days maintained at room temperature (25 °C). The samples were then properly cleaned ultrasonically in acetone for 10 min. Microstructural analyses were then performed in SEM equipped with EDS for the characterization of size, distribution and nature of pores after dezincification.
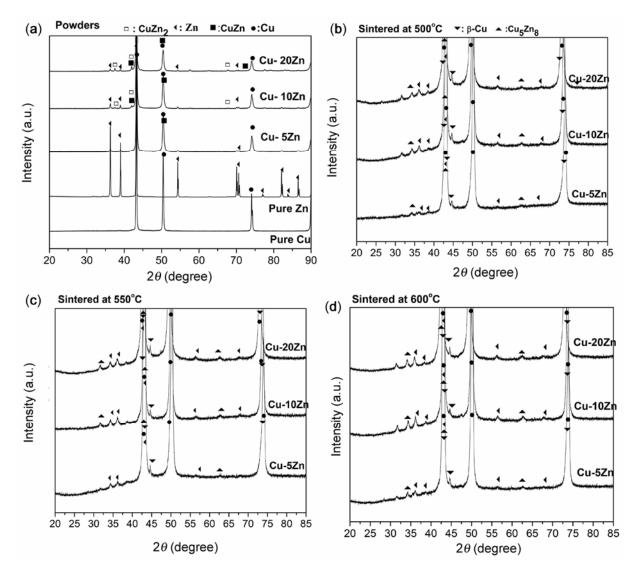

Figure 1. Binary alloy phase diagram of Cu–Zn and the position of the Cu–Zn mixture shown in the figure with arrowhead.

Figure 2. X-ray diffraction patterns of (**a**) ball milled powders of Cu–5 wt% Zn, Cu–10 wt% Zn, Cu–20 wt% Zn mixtures and the pallets sintered at (**b**) 500, (**c**) 550 and (**d**) 600 °C.

3. Results and discussion

Figure 2(a) shows the XRD patterns of the mixed powders after ball milling as well as that of pure Cu and Zn powders. The ball-milled powders show distinct Cu peaks whereas, the Zn peaks are relatively weaker because only 5, 10 and 20 wt% Zn are present in respective powder mixtures. The presence of distinct Cu and Zn peaks in the ball-milled powders shows that pre-dominantly Cu and Zn are present in elemental form in the milled powders. However, the patterns show some additional peaks and this confirms the formation of small fraction of $CuZn_2$ and CuZn phases. This suggests that there is a possibility of reaction between the Zn and Cu particles at the interface region during low energy ball milling. Figures 2(b–d) show the XRD patterns from the spark plasma sintered Cu–Zn aggregates at 500, 550 and 600 °C, respectively.

Analysis of these patterns shows that with increase in Zn content as well as with increase in sintering temperature, new peaks appear. However, elemental peaks of pure Zn and pure Cu still persist suggesting that there are reactions between Cu and Zn at the particle boundaries. Certain intermetallics like Cu_5Zn_8 (cubic), $CuZn_2$ (cubic) and CuZn (rhombohedral) are found in the sintered samples.

Figure 3(a and b) show the variation of density of the sintered samples as a function of temperature and Zn content, respectively. The rate of density change increases with the increase in temperature and Zn content (figure 3a) suggesting better sintering. However, the density of the sintered sample is minimum at lowest temperature with maximum Zn content (20 wt%) and vice versa. Figure 3(c and d) show the variation of relative density of the sintered aggregates as a function of temperature and Zn content, respectively. It is clear from sinterability
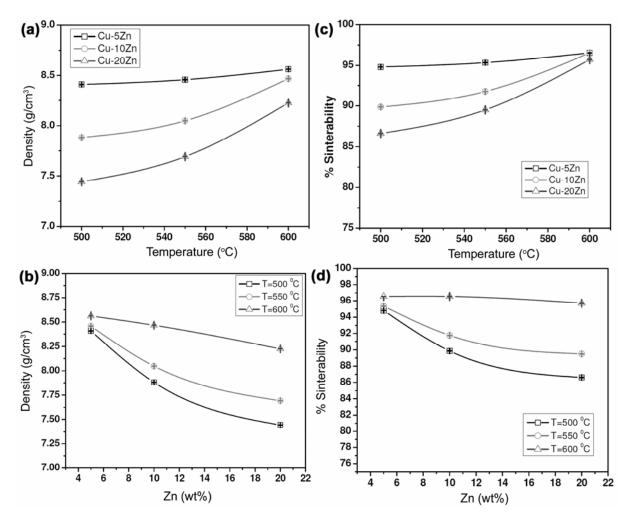
Figure 3. Variation of density and sinterability of the sintered pellets with the variation in (**a**) and (**b**) sintering temperature and (**c**) and (**d**) composition.

plots (figure 3c and d) that the relative sintered density increases with increase in temperature of sintering and density is maximum for lowest Zn content suggesting least porosity content for lowest Zn-content at highest temperature. Hence, despite the tendency of volatile Zn to evaporate at elevated temperature, the densification by inter-diffusion of Cu and Zn atoms possibly predominates with increase in sintering temperature and lower Zn content.

Figure 4(a–c) show the optical micrographs of Cu–5 wt% Zn sintered at 500, 550 and 600 °C, respectively. The colour contrast within the reddish background of the images describes the presence of Zn particles within the Cu matrix (shown by arrowhead). The porosity can be seen to be decreasing with increase in sintering temperature giving rise to a more compact microstructure at higher sintering temperature. Figure 5(a–c) show the SEM micrographs in the secondary electron imaging mode of Cu–10 wt% Zn sintered at 500, 550 and 600 °C, respectively. The dark phases indicate the presence of Cu phases while the bright phases indicate the Zn phases.

Higher densification tendency, i.e. less porosity (shown by arrowhead) at higher sintering temperature is also clearly depicted in the micrographs.
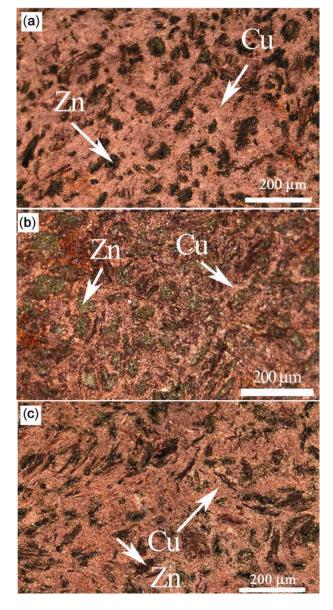
The SEM micrographs of Cu–20 wt% Zn sintered at 500, 550 and 600 °C are shown in figures 6(a–c), respectively. Marked differences in the distributions of solute, i.e. Zn-rich and Cu-rich regions in the microstructures with respect to the sintered samples with lower Zn content are observed. It may be attributed to the higher interfacial area between Cu and Zn resulting into greater reaction possibility and subsequent intermetallics formation at high temperature during sintering in Cu–20 wt% Zn sample. The XRD patterns of the Cu–20 wt% Zn (figure 2) also indicate that the intermetallics formation is more pronounced in higher Zn containing mixtures.

Table 1 shows the point analysis of the sintered samples as indicated in the SEM micrographs (figure 7a–c) for the Cu–5 wt% Zn, Cu–10 wt% Zn and Cu–20 wt% Zn samples sintered at 500 °C, respectively. It confirms the presumption that higher the Zn content, the higher would be the interfacial bonding between Cu and Zn particles

resulting in alloying and homogenization upon sintering. Figure 8(a–c) shows the line scan composition/elemental profiles for Cu and Zn for the Cu–5 wt% Zn samples sintered at 500, 550 and 600 °C, respectively. The localized nature of variation can be seen in the case of 500 and 550 °C sintered samples, while the 600 °C sintered samples, indicate better homogenization of elemental distribution, which reconfirms the distribution of Cu-rich and Zn-rich regions.
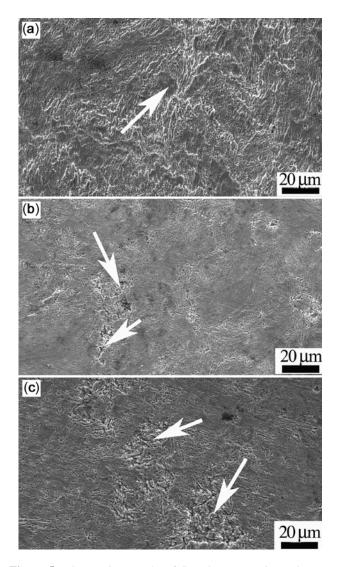
Figure 9(a and b) shows the variation of Vickers hardness with increase in Zn content and sintering temperatures, respectively. The Vickers hardness shows an increasing tendency with increase in Zn content and sintering temperature and is highest for the sample with highest Zn content sintered at highest sintering temperature. Ja-Myeong *et al* (2008) have studied that the addition of 5–30 wt% Zn in pure Cu and demonstrated an increase in hardness by 15–60% along with the increase in grain size. However, in the present case, the hardness increase is about 15%, when the mixture with highest Zn content is sintered at highest temperature.
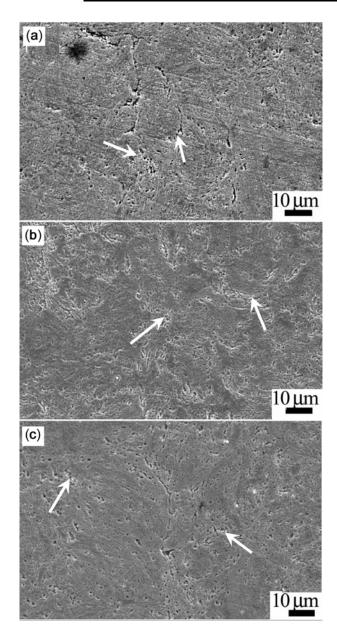
Figure 10 shows the elemental mapping carried out on Cu–5 wt% Zn sintered at 500 °C after immersion test for 45 days in 1 M HCl solution. The image frame corresponding to Zn shows very little X-ray signal providing evidence for complete dissolution of Zn, whereas the image frames for Cu and oxygen indicate the presence of Cu and oxygen all throughout except the pore regions as observed in the SEM micrograph in figure 10. The oxides might have formed due to long exposure to aerated 1 M HCl solution. The remaining Zn (0·25 wt%) obtained from overall area mapping may be present due to Cu–Zn

Figure 4. Optical micrographs of Cu–5 wt% Zn sintered at (**a**) 500 (**b**) 550 and (**c**) 600 °C.

Figure 5. SEM micrographs of Cu–10 wt% Zn sintered at (**a**) 500 (**b**) 550 and (**c**) 600 °C.

Table 1. Compositional analysis (EDS) of the points shown in the micrographs of sintered pellets in figure 7.

Composition	Sintering temperature (°C)	Spectrum	Cu (wt%)	Zn (wt%)
Cu–5 wt% Zn	500	A	100	–
		B	90·33	9·67
		C	86·69	13·31
		D	82·67	17·33
Cu–10 wt% Zn	500	A	84·18	15·82
		B	93·44	6·56
		C	86·94	13·06
Cu–20 wt% Zn	500	A	74·26	25·74
		B	78·61	21·39
		C	81·28	18·72

Figure 6. SEM micrographs of Cu–20 wt% Zn sintered at (**a**) 500 (**b**) 550 and (**c**) 600 °C.

Figure 7. Composition measured from EDS point analysis mentioned in table 1 from the different regions as indicated in SEM micrographs of (**a**) Cu–5 wt% Zn sintered, (**b**) Cu–10 wt% Zn sintered and (**c**) Cu–20 wt% Zn sintered at 500 °C.

Table 2. Compositional analysis (EDS) of the points shown in the micrographs of corroded surfaces of Cu–5 wt% Zn in figure 11.

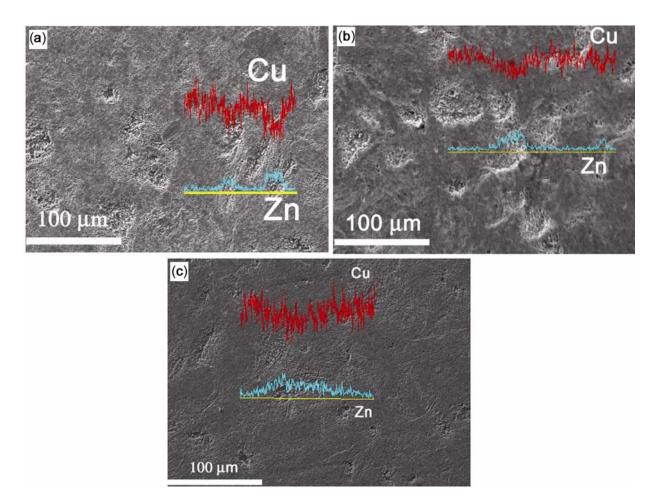| Sintering temperature (°C)	Corrosive used	Spectrum	Cu (wt%)	Zn (wt%)	O (wt%)
500	HCl	A	97·25	0	2·75
		B	98·21	0	1·79
		C	98·04	0	1·96
	NaCl	A	100	0	0
		B	100	0	0
		C	98·55	1·45	0
550	HCl	A	100	0	0
		B	96·1	2·35	1·55
		C	95·57	2·02	2·41
	NaCl	A	79·89	0	20·11
		B	89·14	0	10·86
		C	97·29	0	2·71
600	HCl	A	89·4	10·03	0·58
		B	85·83	7·64	6·53
		C	88·43	6·68	4·89
	NaCl	A	84·71	1·70	13·59
		B	79·88	2·43	17·68
		C	83·07	3·66	13·27

Figure 8. EDS patterns describing line scan analysis of Cu–5 wt% Zn sintered at (**a**) 500 (**b**) 550 and (**c**) 600 °C.
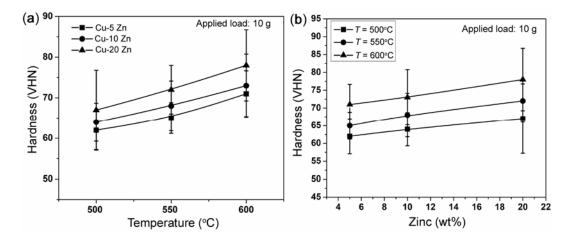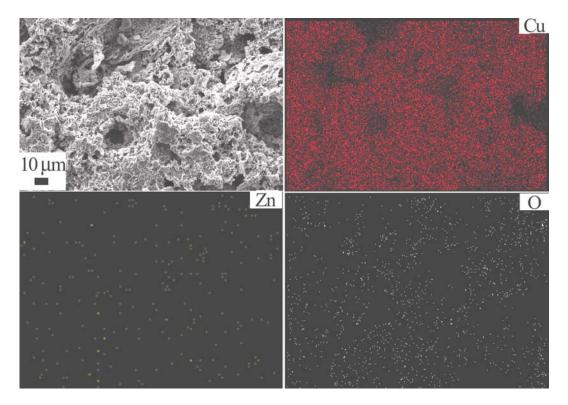
Figure 9. Variation in bulk hardness (Vickers) with respect to (**a**) sintering temperature and (**b**) Zn content.

Figure 10. Mapping of the overall corroded surface area showing elemental distribution of the Cu–5 wt% Zn aggregate sintered at 500 °C immersed in 1 M HCl for 45 days.

intermetallic compounds formed at the interfaces during sintering. Quite a large amount of porosity is observed at few regions.

It is clear that Zn is not present near the pores as observed in the point analysis (table 2) from the regions A, B, and C on the figure 11(a). The evolution of micropores in Cu–5 wt% Zn sintered at 500 and 550 °C upon dissolution in 1 M HCl is shown in figures 11(a and b), respectively. However, in Cu–5 wt% Zn sintered at 600 °C, the dissolution of zinc is not effective according to the

EDS data shown in table 2. Almost complete Zn is retained in the matrix and only overall dissolution from Cu–Zn matrix has occurred. The pore size after dissolution is found to be in the range of 1·5–40 μm with an overall porosity of 39·4, 27·6 and 44% for Cu–5 wt% Zn sintered at 500, 550 and 600 °C, respectively. Extensive dissolution of both Cu and Zn is found to have occurred in those samples sintered at relatively lower temperature, which is being confirmed from EDS analysis as shown in table 2. The surface topography is quite rough and similar
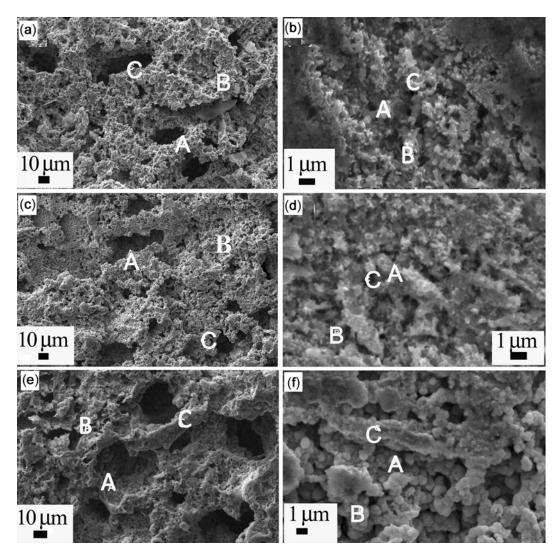
Figure 11. Composition measured from EDS point analysis mentioned in table 2 from the different regions as indicated in SEM micrographs of Cu–5 wt% Zn sintered at (**a**) 500, (**b**) 550 and (**c**) 600 °C all immersed in 1 M HCl for 45 days and (**d**) 500, (**e**) 550 and (**f**) 600 °C all immersed in 3.5 NaCl for 45 days.

for all the samples which may lead to the conclusion that the selective dissolution of the Zn rich regions has taken place (Ahmed and Macdonald 2012) in 1 M HCl solution. The effect of low pH ~ 0·47 (1 M HCl) solution is quite pronounced from the fact that oxide layer formation is strongly prevented (table 2).

Figures 11(d, e and f) shows the surface morphology of Cu–5 wt% Zn sintered at 500, 550 and 600 °C, respectively, after dissolution in 3·5 wt% NaCl solution for 45 days. The points marked as A, B and C, indicate the locations from where the EDS data shown in table 2 are obtained. The Zn content is very low, but at few regions only. Minor amount of Zn dissolution has occurred in Cu–5 wt% Zn sintered at 600 °C shown in figure 11(f). Though, very fine pores have formed, the rate of dissolution is quite slow. Formation of oxide layers on the surface prevents dissolution, although, fine porosity evolution

has occurred penetrating through the oxide films. Pore size ranges from 550 nm to 3 μm. The morphology also indicates that dezincification occurs following selective leaching mechanism in NaCl solution (Ahmed and Macdonald 2012).

Rapid but premature sintering obtained from spark plasma sintering prevents the evaporation of Zn at elevated temperature and results into formation of hard intermetallics only at the interfaces, thereby, forming a network like structure with a hard boundary and a soft matrix from where the anodic dissolution of Zn initiates upon immersion. But, too high solute concentration, as in the case of Cu–20 wt% Zn, may accelerate the formation of intermetallic compounds due to the increased interfacial area between Cu and Zn particles, which enhance the reaction possibility. Thus, the final rate of dezincification phenomena may be retarded due to absence of adequate free

Zn. Thus, optimum amount of Zn (here Cu–5 wt% Zn) is to be chosen for better dissolution. The dissolution test for the alloys with higher Zn content will be taken up for future analysis. In case of the samples immersed in 1 M HCl, extensive corrosion has occurred and from the images, it is clear that selective dissolution (Ahmed and Macdonald 2012) of the Zn phase has just started in the samples immersed in 3·5% NaCl. Less than micron-sized pores as compared to the samples immersed in 1 M HCl are observed on the surfaces of those samples. But, even upon extensive exposure in 3·5 wt% NaCl solution, the selective dissolution of Zn as well as the distribution of pores, is not that much effective with respect to that in 1 M HCl. Formation of oxide layers on the sample surface due to the exposure in aerated solutions, especially in 3·5 wt% NaCl solution, is thought to initially restrict the action of Cl$^-$ ions on free Zn atoms. However, final dissolution occurs by penetrating through the oxide film. It can be easily concluded from the structure that exposure for longer time or in controlled potential would have created more uniform porosity in these samples.

4. Conclusions

Due to spark plasma sintering, the concentration of Zn is maintained exactly and thoroughly as per the initial composition. The hard intermetallics formed during sintering at the Cu–Zn interfaces act as the boundary network. The premature sintering successfully results in formation of hard inter-particle boundaries comprising of intermetallics and pure Cu and Zn have been inside the matrix. Uncontrolled dezincification has occurred from the Cu–Zn matrix through selective leaching mechanism. Low temperature sintering is preferred to avoid the formation of intermetallics in the matrix which would prevent preferential dissolution. The effect of chloride ions from 1 M HCl is much more pronounced than that of 3·5 wt% NaCl, though the pores are comparatively finer in case of NaCl solution than that of HCl solution.

References

Ahmed Z and Macdonald D 2012 *Principles of corrosion engineering and corrosion control* (Oxford, UK: Butterworth-Heinemann) 2nd edn

Bond G C and Thompson D T 1999 *Catal. Rev. Sci. Eng.* **41** 319

Gladen H, Kaiser H and Kaesche H 1990 *Corros. Sci.* **30** 737

Gutmanas E Y 1990 *Prog. Mater. Sci.* **34** 261

Hisashi I, Yoshiharu K, Akimichi Ka, Shufeng Li, Katsuyoshi Kondoh, Junko U and Haruhiko A 2010 *Powder Tech.* **198** 417

Huang J F and Sun I W 2004 *Chem. Mater.* **16** 1829

Hungria Teresa, Galy Jean and Castro Alicia 2009 *Adv. Eng. Mater.* **11** 615

Jagodzinski Yu, Aaltonen P, Smuk S, Tarasenko O and Hanninen H 2000 *J. Alloys Compd.* **310** 256

Ja-Myeong K, Hideki A and Seung-Boo Jung 2008 *Mater. Sci. Eng.* **A483–484** 254

Jia F L, Yu C F, Ai Z H and Zhang L Z 2007a *Chem. Mater.* **19** 3648

Jia F L, Yu C F, Deng K J and Zhang L Z 2007b *J. Phys. Chem.* **C111** 8424

Joo S H, Choi S J, Oh I, Kwak J, Liu Z, Terasaki O and Ryoo R 2001 *Nature* **412** 169

Karpagavalli R and Balasubramaniam R 2007 *Corros. Sci.* **49** 963

Li Z Q, Li B Q, Qin Z X and Lu X 2010 *J. Mater. Sci.* **45** 6494

Newman R C, Meng F T and Sieradzki K 1988 *Corros. Sci.* **28** 523

Pickering H W and Wagner C 1967 *J. Electrochem. Soc.: Electrochem. Sci.* **114** 698

Radomyselskii I D, Baglyuk G A and Mazharova G E 1984 *Poros. Metall.* **255** 56

Rintoul M D, Torquato S, Yeong C, Keane D T, Erramilli S, Jun Y N, Dabbs D M and Akshay I A 1996 *Phys. Rev.* **E54** 2663

Shufeng Li, Hisashi I, Haruhiko A and Katsuyoshi Kondoh 2011a *Mater. Design.* **32** 192

Shufeng Li, Katsuyoshi Kondoh, Hisashi I and Haruhiko A 2011b *Powder Tech.* **205** 242

Sieradzki K and Newman R C 1986 *J. Electrochem. Soc.* **133** 1979

Tuck C D S, Powell C A and Nuttall F 2010 in *Corrosion of copper and its alloys. Shreir's corrosion* (eds) R A Cottis, M J Graham, R Lindsay, S B Lyon, J A Richardson, J D Scantlebury and F H Stott (Amsterdam: Elsevier Academic Press) 4th edn, p. 1937

Yeh F H, Tai C C, Huang J F and Sun I W 2006 *J. Phys. Chem.* **B110** 5215

You T Y, Niwa O, Tomita M and Hirono S 2003 *Anal. Chem.* **75** 2080

Zhang X G, Qi Z, Zhao C C, Wang W M and Zhang Z H 2009 *J. Phys. Chem.* **C113** 13139

Zhang C, Sun J, Xu J, Wang X, Ji H, Zhao C and Zhang Z 2012 *Electrochim. Acta* **63** 302